ADVANCES ON LOW-DIMENSIONALITY FLUID MODELING OF HALL THRUSTER DISCHARGES

17 − 18 − 19 MARCH 2021

Enrique Bello-Benítez and Eduardo Ahedo

Equipo de Propulsión Espacial y Plasmas, Universidad Carlos III de Madrid, Av. de la Universidad, 30, 28911 Leganés, Madrid, Spain.
ebello@ing.uc3m.es

ABSTRACT:

In the past, 1D-axial stationary macroscopic models have been seen to be able to properly capture the main features of a conventional Hall-thruster discharge, in-between the anode-to-cathode region, with small computational cost. In this work, a 1D-axial stationary macroscopic model is proposed, partially based on previous works, keeping effects that allow to better reproduce the physics in the vicinity of the cathode and in the far-plume region. Previous studies highlighted that azimuthal electron inertia effects are important in the vicinity of the cathode. Here, we propose a fluid model for electrons that account for the corresponding terms. The azimuthal inertia cannot be neglected when the electrons eventually demagnetize in the plume, yielding much lower decay of the azimuthal drift than an inertialess model. This can have a direct impact on the performances obtained from the thruster model. An accurate and smooth behavior of the plasma variables in the vicinity of the cathode is achieved by using a finite thickness cathode, modeled as a source of particles and energy in the electron macroscopic equations. In contrast with infinitely thin models used so far, the finite cathode model couples the evolution of the plasma variables in the internal an external regions of the discharge. This requires to solve in a domain extending from the anode sheath edge to an arbitrarily far far-field boundary. Despite its limitations, the 1D axial stationary model provides solutions that are simple to interpret with a small computational effort. We use the model to analyze the role of electron azimuthal inertia, the far-field plasma behavior, the impact of the finite cathode, the effect of a change in the far-field boundary conditions or test different turbulent transport approaches.

1. INTRODUCTION

Hall-effect thrusters (HET) are electric propulsion devices well consolidated in the current market. However, certain physical phenomena are poorly understood and the lack of predictive models is a matter of fact, what makes HET discharge modeling a very active field of research [1, 2].

One of the main challenges is the modeling and characterization of cross-field electron transport due to turbulence and instabilities. There are numerous examples in the recent literature dealing with this matter from different perspectives: macroscopic local [3–5] and global [6–9] stability analyses, local kinetic instabilities [10–12] and particle-in-cell simulations [13–16].

The analysis of axial plasma oscillations in HET discharge has motivated also the recent development of transient 1D axial fluid and hybrid models [17–19]. However, there are no many recent examples of 1D axial stationary models that can be, however, very relevant, e.g., for the analysis of global instabilities. In a very recent article [6], we conducted this type of stability analysis and showed the global dispersion relations resulting for several equilibrium solutions obtained with a 1D axial stationary model of the HET plasma in-between the anode and the cathode. The results prove that the families and characteristics of the obtained instabilities are very dependant on the equilibrium solution and, thus, an accurate description of the axial equilibrium plasma response may be important for a better characterisation of global instabilities. Apart from that, axial stationary models offer great flexibility and low computational effort when it comes to carry out parametric studies and analyze the impact of modeling decisions on the average axial behavior of the discharge, e.g., the role of electron inertia, boundary conditions or turbulent transport models.

In this work, we present a 1D axial stationary model for the HET plasma discharge, whose main novelties with respect previous works [20–22] are the inclusion of inertia in the electron momentum balance and a finite-thickness cathode. While these articles were much more focused on the analysis of the anode-to-cathode region, the new features of the model here allow a more accurate description of the discharge in the vicinity of and past the cathode, where the transition to the unmagnetized plume happens. In contrast with [20–22], the finite cathode model couples the evolution of plasma variables in the interior and exterior regions of the

discharge. Therefore, the solutions to our model are computed on a domain that covers the complete region from the anode sheath-edge to an arbitrarily far downstream boundary.

The formulation of the three-fluid axial stationary model is included in section 2, including a detailed description of the infinitely thin and finite cathode models. Section 3 is devoted to results. A reference nominal solution with parameters partially based on SPT-100-type HET is presented and several effects are discussed: role of electron inertia, effect of the finite cathode model, different turbulent transport approaches and effect of far-field boundary conditions. Finally, conclusions and other considerations are gathered in section 4.

2. MODEL FORMULATION

The axial stationary Hall discharge is modeled in this work as three fluids: neutral, singly-charged ion and electron species (sub-indexes n, i, e; respectively). The model is partially based on previous works by Ahedo et al. [20–22]. There, a quasineutral plasma is considered, with unmagnetized ions, negligibly small pressure force on ion and neutral fluids; and negligible electron inertia. The magnetic field is assumed to have only radial component. The cathode was modeled in [20–22] as an infinitely thin layer where the total axial current changes abruptly from I_d inside the chamber to zero in the plume region (the axial electron velocity changes sign and gets modified accordingly). The general stationary model introduced below includes some additional physical effects, such as a cathode source or azimuthal electron inertia.
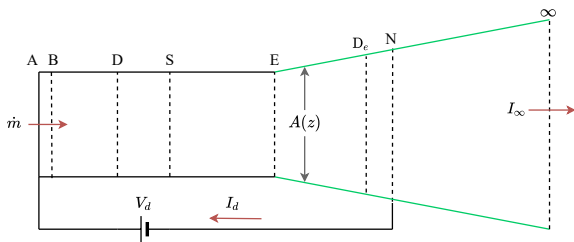

Figure 1: Schematic representation of the plasma discharge structure in a Hall thruster. Hereafter, $\dot{m}$ is the mass flow, V_d is the discharge voltage, I_d the discharge current, and I_∞ is the far-field total current. A is the anode wall, B is the anode sheath edge, D is the ion stagnation point, S is the ion sonic point, E is the chamber exit, D_e is the electron stagnation point, N is the cathode center and ∞ is the far-field downstream boundary. $A(z)$ is the effective cross-section area.

Let us assume axial symmetry and study the axial evolution of plasma variables at the chamber mid-radius (R), with the divergence operator (acting on

an arbitrary vector v) expressed as

$$\nabla \cdot \boldsymbol{v} = \frac{1}{A}\frac{\mathrm{d}}{\mathrm{d}z}(Av_z) + v_w' \qquad \text{(Eq. 1)}$$

where z stands for the axial coordinate, A for the cross-sectional area of the plasma beam and v_w' accounts for contributions from lateral wall fluxes. As shown in figure 1, the simulation domain includes the complete plasma region in-between the anode sheath edge (B) and an arbitrarily far downstream boundary (∞). The point A stands for the real anode wall, which has attached an infinitely thin non-neutral sheath from A to B. The thruster exit is located at point E ($z = L_E$) and the cathode is centered at point N ($z = L_N$). The distance from N to the ∞ is $L_{N\infty}$. The azimuthal flows are assumed to be important only for electrons and the radial velocity components are disregarded. The macroscopic equations, under these assumptions and following a standard notation, read

$$\frac{1}{A}\frac{\mathrm{d}}{\mathrm{d}z}(An_nu_{zn}) = -n(\nu_p - \nu_w), \qquad \text{(Eq. 2)}$$

$$\frac{1}{A}\frac{\mathrm{d}}{\mathrm{d}z}(Anu_{zi}) = n(\nu_p - \nu_w), \qquad \text{(Eq. 3)}$$

$$\frac{1}{A}\frac{\mathrm{d}}{\mathrm{d}z}(Anu_{ze}) = n(\nu_p - \nu_w) + S_c, \qquad \text{(Eq. 4)}$$

$$m_in_nu_{zn}\frac{\mathrm{d}u_{zn}}{\mathrm{d}z} = m_in[\nu_w(u_{znw} - u_{zn}) \\ + \nu_{in}(u_{zi} - u_{zn})] \quad \text{(Eq. 5)}$$

$$m_inu_{zi}\frac{\mathrm{d}u_{zi}}{\mathrm{d}z} = -en\frac{\mathrm{d}\phi}{\mathrm{d}z} \\ + m_in\nu_i(u_{zn} - u_{zi}), \quad \text{(Eq. 6)}$$

$$0 = -\frac{\mathrm{d}p_e}{\mathrm{d}z} + en\frac{\mathrm{d}\phi}{\mathrm{d}z} + eBnu_{ye} - m_en\nu_eu_{ze}, \quad \text{(Eq. 7)}$$

$$m_enu_{ze}\frac{\mathrm{d}u_{ye}}{\mathrm{d}z} = -eBnu_{ze} - m_en\nu_eu_{ye}, \quad \text{(Eq. 8)}$$

$$\frac{1}{A}\frac{\mathrm{d}}{\mathrm{d}z}\left[A\left(\frac{5}{2}nT_eu_{ze} + q_{ze}\right)\right] = u_{ze}\frac{\mathrm{d}p_e}{\mathrm{d}z} \\ - n\nu_pE_{inel} - n\nu_{we}T_e + m_en\nu_eu_e^2 + S_cE_c, \quad \text{(Eq. 9)}$$

$$q_{ze} = -\frac{5p_e}{2m_e\nu_e}\frac{1}{1+\chi^2}\frac{\mathrm{d}T_e}{\mathrm{d}z}, \qquad \text{(Eq. 10)}$$

where ν_p is the production frequency due to ionization, ν_w particle wall-loss frequency, S_c a volumetric source of cathode electrons, u_{znw} is the effective axial velocity of wall-born neutrals, ν_{in} is the charge-exchange collision frequency, $\nu_i = \nu_{in} + \nu_p$ is the total ion collision frequency, ϕ is the electrostatic potential, B is the magnitude of the magnetic field (assumed purely radial), ν_e is the total electron

collision frequency, E_inel is the effective ionization-plus-excitation energy, ν_{we} is the frequency of energy wall losses, E_c is a cathode emission energy, $\chi = \omega_{ce}/\nu_e$ is the Hall parameter, ω_{ce} is the electron gyrofrequency and $p_e = nT_e$. After [20], the plasma plume expansion is accounted for through the expansion law $\mathrm{d}A/\mathrm{d}z = 4\pi R(T_{eE}/m_i)^{1/2}/u_{zi}$. The plasma beam cross-sectional area is constant inside the chamber. All auxiliary models for collisional terms come from previous works [20–22] and are compiled in an appendix of [6]. The axial heat transport equation (Eq. 10), that is a Fourier-type law, comes the vector equation [23]

$$0 = \frac{5}{2}p_e\nabla T_e + e\boldsymbol{q}_e \times \boldsymbol{B} + m_e\nu_e\boldsymbol{q}_e, \qquad \text{(Eq. 11)}$$

after eliminating the azimuthal heat flow q_{ye} from the system.

The magnetic field magnitude is assumed to have a Gaussian shape

$$B(z) = B_m \exp\left[-\frac{(z - z_m)^2}{L_m^2}\right], \qquad \text{(Eq. 12)}$$

being B_m the maximum magnetic field, z_m the location of that maximum and L_m the characteristic length of magnetic decay. Let us note that, in general, different values of L_m are used for the internal ($L_{m,\text{in}}$) a the external ($L_{m,\text{out}}$) regions.

The electron collision frequency include several contributions, such that $\nu_e = \nu_{en} + \nu_{ei} + \nu_{wm} + \nu_t$. Here, ν_{en} is the electron-neutral elastic collision frequency, ν_{ei} is the Coulomb collision frequency (with negligible effect on ion momentum), ν_{wm} accounts for near-wall conductivity. The turbulent transport is modeled as and additional collisional contribution [20, 24] $\nu_t(z) = \alpha_t(z)\omega_{ce}(z)$, where ω_{ce} is the electron gyrofrequency and α_t is a phenomenological profile (not necessarily constant [25, 26]). Unless stated otherwise, we will use a constant value $\alpha_t(z) = 0.0094$.

As already identified in [20], there may be singularities at sonic points, where $u_{zi}^2 = c_s^2$; being $c_s = \sqrt{T_e/m_i}$. Equations (Eq. 2)-(Eq. 10) can be combined to obtain

$$m_i\left(c_s^2 - u_{zi}^2\right)\frac{\mathrm{d}u_{zi}}{\mathrm{d}z} = G, \qquad \text{(Eq. 13)}$$

with

$$\begin{aligned}
G = {} & T_e\left(\nu_p - \nu_w\right) - eBu_{zi}u_{ye} - u_{zi}T_e\frac{\mathrm{d}\ln A}{\mathrm{d}z} \\
& + m_i\nu_i u_{zi}\left(u_{zi} - u_{zn}\right) \\
& + m_e\nu_e u_{zi}u_{ze} + u_{zi}\frac{\mathrm{d}T_e}{\mathrm{d}z}, \quad \text{(Eq. 14)}
\end{aligned}$$

where $\mathrm{d}T_e/\mathrm{d}z$ is directly given by (Eq. 10). In a conventional solution [20], two sonic points are found in the discharge: at the anode-sheath edge (point B) and an interior sonic transition (point S). The first one is at one of the boundaries and is singular, while for the second one only smooth solutions have physical sense. For point S to be a regular sonic point, necessarily, $G_S = 0$.

Differently to [20–22], we find another possible singularity in (Eq. 8) when $u_{ze} = 0$, as a consequence of having introduced the azimuthal electron inertia. We can expect an electron stagnation point in the vicinity of the cathode (point D_e), since electrons move mostly inwards in the chamber and mostly outwards in the far-field plume. The regularizing condition is, in this case, $u_{ye} = 0$ at D_e.

From the sheath model used in [20], the potential drop from B to A reads

$$\phi_\text{AB} = \frac{T_{e\text{B}}}{e}\ln\frac{\bar{c}_{e\text{B}}}{4|u_{ze\text{B}}|}, \qquad \text{(Eq. 15)}$$

where $\bar{c}_e = \sqrt{8T_e/\pi m_e}$ is the electron thermal velocity. The heat flux at the anode sheath edge follows [21]

$$q_{ze\text{B}} = n_\text{B}u_{ze\text{B}}\left(e\phi_\text{AB} - \frac{1}{2}T_{e\text{B}}\right). \qquad \text{(Eq. 16)}$$

Above equations are solved with the following boundary conditions: (i) total mass flow $\dot{m}$ the anode, (ii) neutral injection velocity at the anode $u_{zn\text{A}} = u_{zn\text{B}}$, (iii) ions have sonic speed $u_{zi\text{B}} = -c_{s\text{B}}$ at B, (iv) reference potential value at the anode $\phi_\text{A} = 0$ that is translated to B as $\phi_\text{B} = \phi_\text{A} + \phi_\text{AB}$, (v) the anode-sheath edge heat flow $q_{ze\text{B}}$, (vi) the discharge potential $\phi_\text{N} = -V_d$ at the cathode, (vii) $G_\text{S} = 0$ at the interior regular sonic point, (viii) the regularizing condition $u_{ye} = 0$ at point D_e and (ix) the far-field electron temperature $T_{e\infty}$ or, alternatively, its gradient $(\mathrm{d}T_e/\mathrm{d}z)_\infty$.

2.1. CATHODE MODEL

Infinitely thin model

The infinitely thin cathode model used in [20–22] considers separately, the interior region (from point B to N$^-$) from the exterior one (from point N$^+$ to ∞)[1]. In addition, there is no electron source term (i.e., $S_c = 0$) in the equilibrium equations. The interior problem is decoupled from the plume past the cathode and is solved from B to N$^-$ with the same boundary conditions of the previous section, except for the following two. The regularizing boundary condition (viii) at the electron stagnation point (i.e.,

---

[1]Points N$^+$ and N$^-$ are considered to be located immediately after and before point N, respectively.

$u_{ye} = 0$ when $u_{ze} = 0$) is not required and is substituted by $u_{yeN^-} = 0$ (note that $u_{zeN^-} \neq 0$). And the condition (ix) is substituted by the value of T_{eN^-}.

The exterior problem is solved with boundary conditions at N^+ that guarantee the continuity at point N of every plasma variable, except for u_{ze} and q_{ze}. The value of u_{zeN^+} is set according to the desired value of the downstream total current I_∞, i.e.,

$$u_{zeN^+} = u_{ziN^+} - \frac{I_\infty}{en_{N^+}A_{cN^+}}. \qquad \text{(Eq. 17)}$$

being I_∞ the far-field plume axial current. Let us note that the total current is spatially conserved, if there is nor cathode particle source, in the interior and exterior regions, independently. For a current-free plume, $u_{zeN^+} = u_{ziN^+}$. The far-field boundary condition (ix) is also used and determines the value of q_{zeN^+}.

Finite thickness model

Subtractring equations (Eq. 3) and (Eq. 4) and multiplying times the unit charge (e), yields

$$\frac{\mathrm{d}I}{\mathrm{d}z} = -eAS_c, \qquad \text{(Eq. 18)}$$

where

$$I = eAn(u_{zi} - u_{ze}) \qquad \text{(Eq. 19)}$$

stands for the total current. Therefore, the variation of I is produced exclusively by the cathode term. Far from the cathode, where $S_c \approx 0$, the total current is constant. This equation can be integrated from the anode to the far-field to get

$$I_d - I_\infty = \int_{z_A}^\infty \mathrm{d}z \; eA(z)S_c(z), \qquad \text{(Eq. 20)}$$

being $z_A \approx z_B$, I_d the discharge current and I_∞ the plume downstream current. The value of I_∞ will be treated as a parameter of the problem, and generally equal to zero for a conventional current-free plume. Since, the discharge voltage V_d is used as boundary condition to fix the potential at point N, the value of I_d is a result. Let us decide that the cathode charge emission is concentrated close to point N and follows a Gaussian evolution

$$eA(z)S_c(z) = K_g \exp\left[-\frac{(z - L_N)^2}{L_g^2}\right] \qquad \text{(Eq. 21)}$$

where K_g and L_g are constants. The value of L_g is intrinsically related to the cathode effective emission thickness l_c and, thus, $L_g = l_c/2$ is a meaningful choice. The integral in equation (Eq. 20) can be computed analytically, assuming that $(L_N - z_A) \gg l_c$; and K_g can be computed from this expression as a function of $I_d - I_\infty$ and l_c. The resultant cathode volumetric source term reads

$$S_c(z) = \frac{2}{\sqrt{\pi}} \frac{I_d - I_\infty}{el_c A(z)} \exp\left[-4\frac{(z - z_N)^2}{l_c^2}\right]. \qquad \text{(Eq. 22)}$$

This cathode source model produces a change in the axial current equal to $I_d - I_\infty$.

3. RESULTS

The model introduced in the previous sections has an important number of parameters that are summarized in the table 1. These values are used through the cases shown in the article, unless stated otherwise. In addition, we will take Xenon as propellant. As noted in this table, the nominal far-field boundary condition is chosen to be the gradient $(\mathrm{d}T_e/\mathrm{d}z)_\infty = 0$ rather than $T_{e\infty}$. We expect that, in the far-field plume, the plasma is substantially homogeneous. Directly related to this, the value of $L_{N\infty}$, that determines how far the far-field boundary condition is imposed, should be taken, ideally, large enough so that the solution becomes independent of $L_{N\infty}$ (next subsection is devoted to this issue).

Table 1: Nominal simulation case parameters, based on a SPT-100-type Hall thruster, used in this work and defined in the main text. $A_{c,in}$ is the chamber cross-section area.

$\dot{m}$	4.75 mg s^{-1}	V_d	300 V
B_m	247 G	z_m	2.5 cm
$A_{c,in}$	40 cm^2	R	4.25 cm
u_{znB}	300 m s^{-1}	$(\mathrm{d}T_e/\mathrm{d}z)_\infty$	0
I_∞	0	l_c	1 cm
E_c	7.5 eV	$L_{N\infty}$	40 cm
L_E	2.5 cm	L_N	3.35 cm
$L_{m,in}$	1.5 cm	$L_{m,out}$	0.5 cm

The axial evolution of some relevant plasma variables, solution to the HET discharge model with parameters in table 1, are shown in figure 2. Let us note that $L_{N\infty} = 40$ cm is used for the calculations, but for the figure the abscissa limits are chosen to have a clearer view of the much more inhomogeneous evolution within the thruster chamber.

Inside the chamber, an ion-backstreaming region is identified between points B (left boundary) and the ion-stagnation point D. Ions are generated in the middle of the plasma discharge due to ionization and some of them move together with electrons towards the anode, since, naturally, the plasma tends to be quasineutral. The electric field E_z is small and points towards the anode here. The main ionization region can be identified to be in-between D and the ion-sonic point S, where the ion flow is subsonic and the plasma density peak takes place (see figure 2(a)). The most significant ion acceleration happens in-between points S and N (see figure 2(b)), where there is the largest potential drop. Consequently, ions become highly supersonic and plasma density

decreases due to the acceleration of the ion flow. From N to ∞ (right boundary), there is an slight potential rise that decelerate the ions. Although barely noticeable in figure 2(d), after plasma is approximately demagnetized, the supersonic expansion of the plume results in a mild acceleration of the ions. The conservation of the ion particle flux in the plume requires a decay of plasma density.
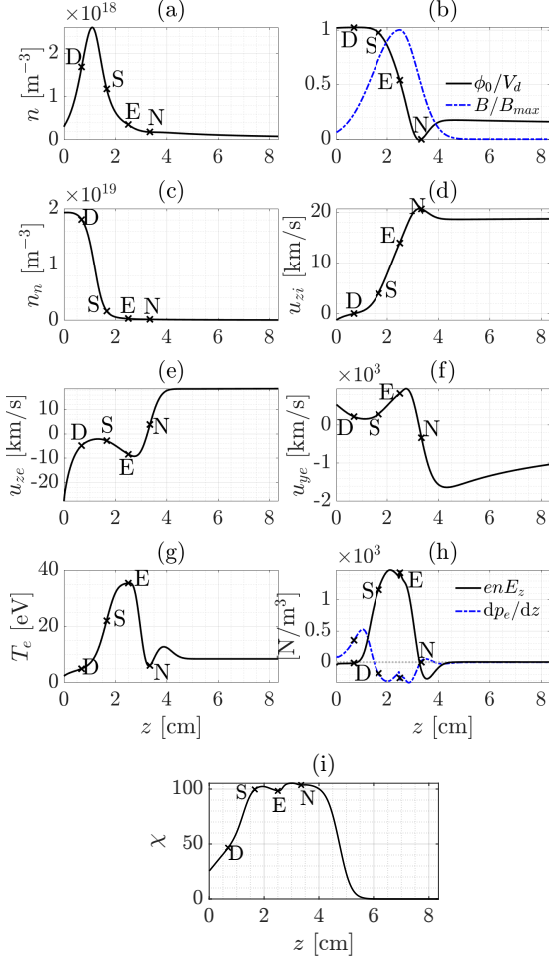

Figure 2: Stationary axial response for parameters in Table 1. Ion-stagnation (D), ion-sonic (S) and channel exit (E) are marked with crosses. Only $B(z)$ is an input, its maximum being at E.

Looking now at electron variables, the electron flow is heated, starting at N, both inwards and outwards mostly due to Joule heating, that competes with lateral-wall energy losses. In the chamber, a maximum T_e is reached close to the exit (point E) and electrons flow is cooled from E to the anode due, mainly, to the energy expended in ionization. Let us note that the sign of dT_e/dz is governed by the sign of q_{ze}. In the far-field plume, the temperature stabilizes around $T_{e\infty} = 8.4$ eV, and the electron axial momentum (Eq. 7) and energy (Eq. 9) equations can be approximately simplified to

$$0 = -T_e \frac{dn}{dz} + en \frac{d\phi}{dz} \qquad \text{(Eq. 23)}$$

and

$$\frac{1}{A} \frac{d}{dz} \left[A \left(\frac{5}{2} n_0 T_{e0} u_{ze0} + q_{ze0} \right) \right] =$$
$$u_{ze0} T_e \frac{dn}{dz}, \quad \text{(Eq. 24)}$$

respectively; where we neglected the temperature gradient compared to the density one. After integration, (Eq. 23) yields a Boltzmann-type relation.

Let us note that (Eq. 23) can be interpreted as the conservation of mechanical energy while, on the other hand, (Eq. 24) is the internal energy balance. The work of the pressure force appears in both equations as a term taking the electron thermal energy flux and expending it into electric field work. At the same time, this electric field produces the acceleration of ions in the expanding plume. From an energetic point of view, the electron thermal energy is converted into ion kinetic energy.

Inside the thruster and part of the near plume, electrons move axially towards the anode, while they move downstream in the plume past the cathode. If the cathode source is adjusted, as explained in section 2.1., for $I_\infty = 0$, in the far-field, necessarily, the electrons move with $u_{ze} = u_{zi}$, in a quasineutral plasma. Therefore, there is, macroscopically a change of sign in u_{ze}, that is produced by the cathode. The azimuthal velocity u_{ye} is the result, inside the thruster and in the magnetized plume, of $\boldsymbol{E} \times \boldsymbol{B}$ and diamagnetic drifts (see equation (Eq. 7), without the collisional term). The electric and pressure forces associated to these phenomena, respectively, are plotted in figure 2(h). Clearly, the diamagnetic contribution dominates near the anode , while the $\boldsymbol{E} \times \boldsymbol{B}$ is dominant in the rest of the chamber and near-plume. The azimuthal momentum balance requires that the change of sign of u_{ze} goes with a change of sign of u_{ye}. Mathematically, this is required to have a non-singular electron stagnation point. In the unmagnetized plume, the physics are quite different and the evolution of u_{ye} is governed by (Eq. 8) (of course, without magnetic term). This is, the collisions should progressively attenuate u_{ye}. This evolution is however quite slow, compared to other variables, in the solution shown in figure 2.

The rate of decay of $|u_{ye}|$ is intrinsically related to $T_{e\infty}$ through $\nu_{e\infty}$. As noticed in coming sections, the value of $T_{e\infty}$ is much more sensitive to changes in the model and parameters than $n_{n\infty}$ and n_∞. The evolution of $\nu_{e\infty} \approx \nu_{ei\infty} + \nu_{en\infty}$ with $T_{e\infty}$, taking fixed reference values $n_{n\infty} = n_\infty = 10^{17}$ m^{-3}, is as plotted in figure 3. The net collision frequency has a minimum at $T_{e\infty} \approx 26$ eV. For the reference case of figure 2, a colder plume would result into a faster decay of $|u_{ye}|$ in the plume.
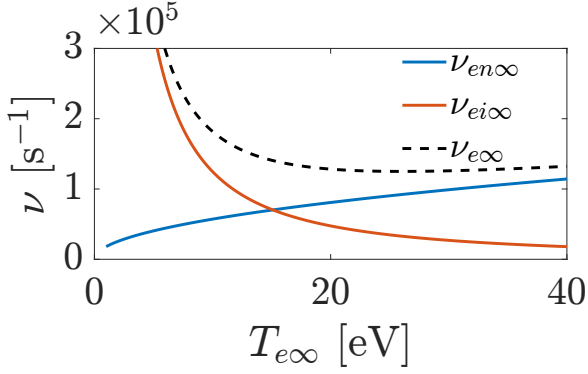
5

Figure 3: Evolution of the far-field electron collision frequency $\nu_{e\infty}$ with $T_{e\infty}$ for reference values $n_{n\infty} = n_\infty = 10^{17}$.

For the next part of the article, changes in the parameters and in the model itself are considered. In every case, we decided to keep constant the value of n_B, by changing B_m accordingly. This is motivated by numerical difficulties found in some calculations (mainly when trying to get solutions with no turbulent transport, i.e., $\alpha_t(z) = 0$). The obtained values of B_m and other characteristic magnitudes are included in table 2.

Table 2: Characteristic values for the different considered cases throughout the article. The value of B_m is such that n_B is kept constant for all cases. After [21], the value of the thrust F takes into account the contribution of azimuthal plasma current in the plume.

Case	B_m [G]	F [mN]	I_d [A]	I_{eB} [A]	$I_{i\infty}$ [A]
nominal	247	81.9	5.19	5.44	2.95
$L_{N\infty} = 10$ cm	247	82.9	5.19	5.44	3.06
$l_c = 0$	216	80.5	5.24	5.49	2.94
inertialess	245	81.2	5.17	5.43	2.95
$\alpha_t(z) = 0$	92	78.6	4.29	4.54	2.94
rippled $\alpha_t(z)$	231	83.1	5.14	5.40	2.95
$T_{e\infty} = 1$ eV	247	82	5.18	5.43	3.07

3.1. SOLUTION DEPENDENCE ON $L_{N\infty}$

As aforementioned, $L_{N\infty}$ should be taken big enough so that the solution is independent of its value. Figure 5 shows some relevant profile solutions for values $L_{N\infty} = 40$ cm (reference case) and $L_{N\infty} = 10$ cm. The solutions match almost perfectly in region from B to N. In the plume past the cathode, some profiles are in good agreement (e.g., ϕ and n). However, u_{ye} and T_e have been realized to be more sensitive to $L_{N\infty}$. To be precise, the value of $T_{e\infty}$ is 11.6 eV for the case with $L_{N\infty} = 10$ cm, while it is 8.4 eV in the reference case. These values have a direct impact on $\mathrm{d}u_{ye}/\mathrm{d}z$ in the far-field. In fact, the slower decay of $|u_{ye}|$ in the off-nominal case is consistent with figure 3.

The value of $T_{e\infty}$ seems a good indicator that the solution is independent of $L_{N\infty}$. We have repeated the calculations for several values of $L_{N\infty}$. The evolution of $T_{e\infty}$ with $L_{N\infty}$ is represented in figure 4. An asymptotic behaviour can be suspected with the asymptote at around $T_{e\infty} = 8$ eV. Although there is some dependence of the solution on $L_{N\infty}$ for the reference value of 40 cm, we consider it a reasonable trade-off between accuracy and computational time (larger $L_{N\infty}$ implies more points required for the numerical grid and, thus, more computing workload).
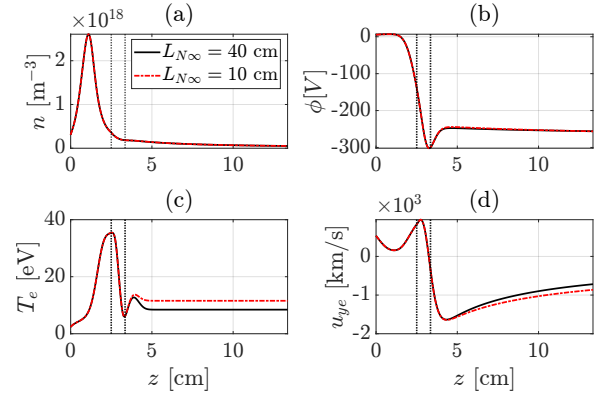

Figure 4: Stationary axial response of reference case (black solid line) and with $L_{N\infty} = 10$ cm (red dash-dotted line). Black dotted vertical lines denote, from left to right, respectively, the location of the exit (point E) and the cathode center (point N).
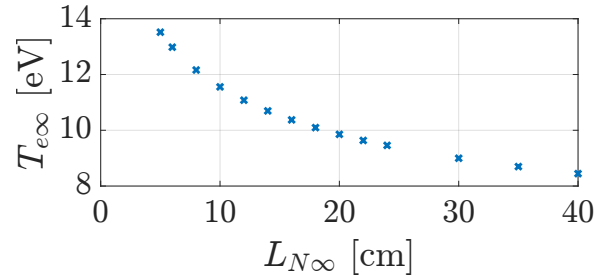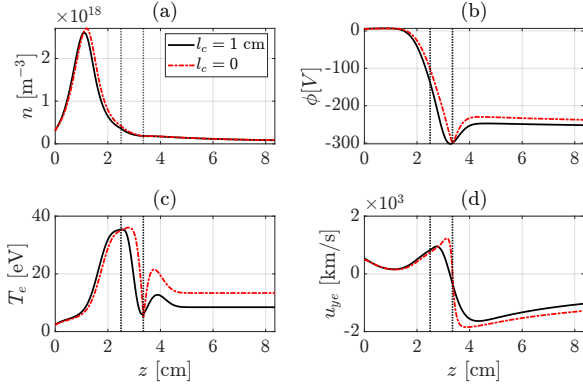

Figure 5: Evolution of $T_{e\infty}$ with the parameter $L_{N\infty}$.

3.2. ANALYSIS OF CATHODE EFFECTIVE THICKNESS

In this section, let us compare the reference solution with the case of an infinitely thin cathode (see figure 6). As explained in section 2.1., in the infinitely thin case, the cathode model used for the reference case becomes singular. Therefore, the cathode has to be modeled as boundary conditions, having interior and exterior decoupled regions and allowing discontinuities in $u_{ze}(z)$ and $q_{ze}(z)$ at point N. Moreover, every other profile solution is neither differentiable at point N. A finite cathode smooths these profiles in the vicinity of the cathode. The general behaviour of both solutions is similar, but the effect of the cathode cannot be disregarded.

Apart from the impact on stationary solutions, having a cathode model may be relevant for global stability analyses such as those of references [6, 9]. In [6] we studied global instabilities in Hall thrusters using an infinitely thin cathode for the equilibrium model. With a finite cathode, the interior and exterior regions are mathematically coupled what would allow to extent this analysis to the plume past the cathode. Moreover, some near-plume instabilities found in [6] brought up the necessity of a finite cathode model and extending the domain into the downstream plume.

Figure 6: Stationary axial response of reference case (black solid line) with infinitely cathode (red dash-dotted line). Black dotted vertical lines denote, from left to right, respectively, the location of the exit (point E) and the cathode center (point N).

3.3. ANALYSIS OF ELECTRON INERTIA

A novelty of the presented model with respect to previous works [20–22] is the inertia term in the left-hand side of equation (Eq. 8). In this section we evaluate the relevance of azimuthal inertia in the discharge. If that term is disregarded, equation (Eq. 8) gets simplified to

$$0 = -eBnu_{ze} - m_e n\nu_e u_{ye}, \qquad \text{(Eq. 25)}$$

which can be rewritten as

$$u_{ye} = -\frac{\omega_{ce}}{\nu_e}u_{ze} = -\chi u_{ze}. \qquad \text{(Eq. 26)}$$

Let us note that, in the inertialess case, the points having $u_{ze} = 0$ are no longer singular and the model does need boundary condition (vii). Even so, according to the previous expression, the inertialess solution still satisfies that $u_{ye} = 0$ when $u_{ze} = 0$. The existence of the electron stagnation point is closely related to the finite cathode model, that movitates a change of sign of u_{ze}.

The inertialess and reference cases are compared in figure 7. Both solutions are in good agreement for most variables. Regarding u_{ye} the two profiles show good matching in the interior region from B to N, but

the evolution in the downstream plume is completely different. This is because, in the inertialess model, the value of u_{ye} is tied to the the magnitude of the magnetic field, as in (Eq. 26), because the magnetic and collisional forces are the only terms in the azimuthal momentum balance. However, this model is not suitable for unmagnetized regions of the plume, where inertia cannot be neglected and is able to balance the collisional force.
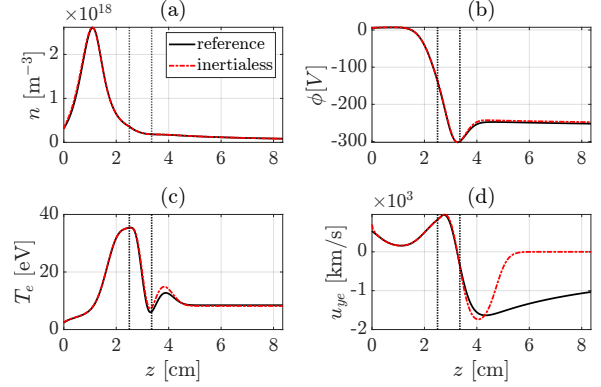

Figure 7: Stationary axial response of reference case (black solid line) and inertialess solution (red dash-dotted line). Black dotted vertical lines denote, from left to right, respectively, the location of the exit (point E) and the cathode center (point N).

In reference [6], we compared solutions with and without azimuthal inertia, in the region from B to N and having an infinitely thin cathode. Those results, in the interior region close to point N, were not in as good agreement as those in figure 7(d). In an inertialess model, the effect of the finite cathode partially mitigates the lack of electron inertia in the vicinity of point N.

3.4. ANALYSIS OF THE TURBULENT PARAMETER α_t

The analysis and understanding of turbulence and instablities in Hall thrusters [4, 6, 7, 14, 15, 27–30] (and plasmas under $E \times B$ fields) is a very active field of research since is crucial for the achievement of predictive numerical codes. As aforementioned, the stationary model considered here models anomalous transport using and additional contribution $\nu_t(z) = \alpha_t(z)\omega_{ce}(z)$ and we have considered, so far, $\alpha_t(z) = 0.0094$. In this section we consider two additional cases: absence of anomalous collisions (i.e., $\alpha_t(z) = 0$) and oscillatory $\alpha_t(z)$.

First, the comparison between the reference and the case with constant $\alpha_t(z) = 0$ is plotted in figure 8. Numerical difficulties were found when trying to set $\alpha_t(z) = 0$ keeping the same value of B_m. These difficulties, however, can be explained physically by the fact that reducing the turbulent contribution to ν_e leads to a more effective magnetic confinement of

electrons. Consequently, it is more complicated for the cathode electrons to reach the anode and electron density tends to decrease substantially. In order to overcome these problems, we decided to fix the anode density n_B and let B_m to change accordingly. When $\alpha_t(z) = 0$, this approach results in a substantially weaker magnetic field having $B_m = 92$ G (compared to the reference $B_m = 247$ G). Nevertheless, the maximum Hall parameter increases from $\chi = 105$, in the reference case, to $\chi = 2450$. Therefore, as it should, electrons are much better confined when disregarding the anomalous collisionality. A measure of the poorer cross-field electron transport is the axial electron current $I_e = -enAu_{ze}$ reaching the anode; that decreases from 5.4 to 4.5 A when setting $\alpha_t = 0$ (see table 2). That is to say, without the turbulent contribution the electron current that can be extracted from the cathode has decreased significantly by almost 1 A.

Other side effects of the smaller B_m are the displacement of the ionization region towards the exit (see the peak densities in figure 8(a)) and a shortening of the acceleration region (the decay of ϕ happens within a thinner region in 8(b)). Also the values of u_{ye} near the exit are much more exaggerated so that the axial magnetic force in (Eq. 7) is able to balance the electric one (that is similar in both cases) with a weaker magnetic field.
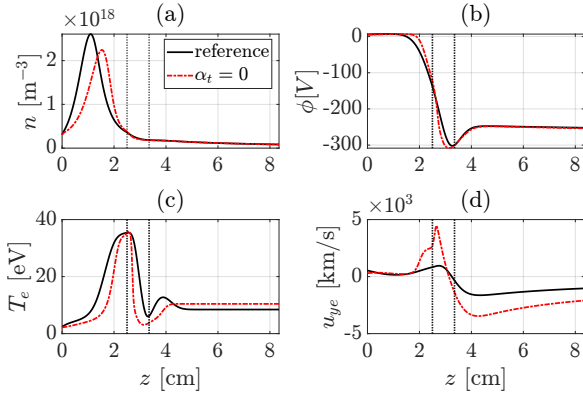

Figure 8: Stationary axial response of reference (black solid line) and $\alpha_t(z) = 0$ cases (red dash-dotted line) given by (Eq. 27) (red dash-dotted line). Black dotted vertical lines denote, from left to right, respectively, the location of the exit (point E) and the cathode center (point N).

On the other hand, azimuthal plasma oscillations are currently considered to be one of the main contributions to electron cross-field transport. The oscillations produce turbulent force contributions to the azimuthal momentum balance that enhances the axial drift of electrons. However, plasma waves in the Hall discharge have, in general, an axial component. Therefore, the turbulent force can be expected to be oscillatory in the axial direction, what

would result in an oscillatory $\alpha_t(z)$. Some examples have been reported in numerical simulations [6, 15]. In figure 9, we consider

$$\alpha_t(z) = \alpha_{t0} + \alpha_{t1} \cos\left(\frac{8\pi}{L_E}z\right), \qquad \text{(Eq. 27)}$$

(with $\alpha_{t0} = 0.0094$ and $\alpha_{t1} = \alpha_{t0}/2 = 0.0047$), and compare it with the reference case. As discussed in [6], an axially rippled turbulent term is expected to enhance the role of azimuthal electron inertia. Moreover, the inertialess model can even fail if $\alpha_t < 0$ within certain region and ν_t is such that $\nu_e < 0$, what could result in electron backstreaming (these type of $\alpha_t(z)$ profiles are not considered here and are left for future work). For this reason the inertialess solution with oscillatory α_t is also computed.
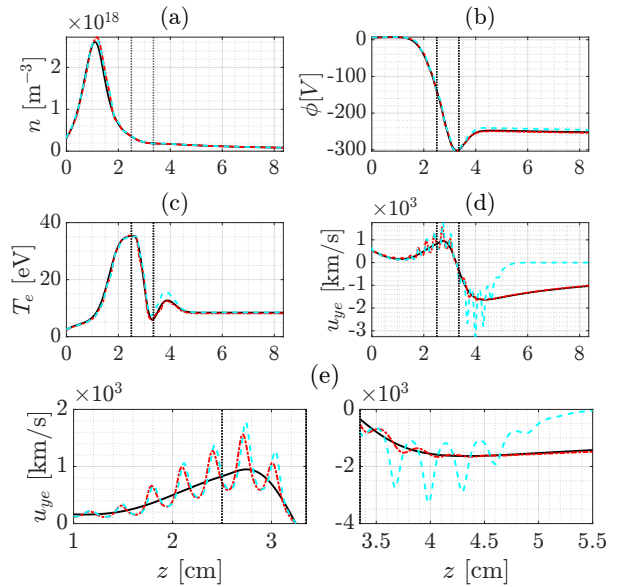

Figure 9: Stationary axial response of reference case (black solid line) and case having $\alpha_t(z)$ given by (Eq. 27), with (red dash-dotted line) and without (blue dashed line) azimuthal electron inertia. Black dotted vertical lines denote, from left to right, respectively, the location of the exit (point E) and the cathode center (point N). Included enlargement of (d) in the vicinity of the cathode (e).

The reference and rippled-α_t solutions follow the same tendency except for the spatial rippling on the plasma variables. These axial oscillations are present in every variable but are more prominent in u_{ye}. The rippling of u_{ye} implies larger du_{ye}/dz and a more significant contribution of the inertia term in (Eq. 7).

The discrepancies in the far field between the solutions with and without inertia were already discussed in section 3.3.. Regarding the behavior of the solutions in the near-cathode region (see figure 9(e)), the electron inertia introduces two effects: damping of u_{ye} oscillations and certain lag between

ripples of u_{ye} and α_t. These are even more evident just past the cathode, where the inertialess solution has much larger amplitude ripples.

3.5. ANALYSIS OF ELECTRON ENERGY FAR-FIELD BOUNDARY CONDITION

Here, we analyze the effect of a far-field boundary condition $T_{e\infty} = 1$ eV (instead of $(dT_{e\infty}/dz)_\infty = 0$) in, figure 10. The solution in the interior part of the discharge seems to be quite independent of the imposed far-field condition. In the plume, the most remarkable differences are the value of the plume electron temperature $T_{e\infty}$ and the evolution of u_{ye}. As highlighted several times, these two are intimately related through the electron collision frequency $\nu_{e\infty}$ in the plume. Figure 3 represents this relation for characteristic values of n_∞ and $n_{n\infty}$. When imposing $T_{e\infty} = 1$ eV, according to this graph, the electron collisionality level in the plume is higher and, thus, $|u_{ye}|$ decays faster than in the reference case.
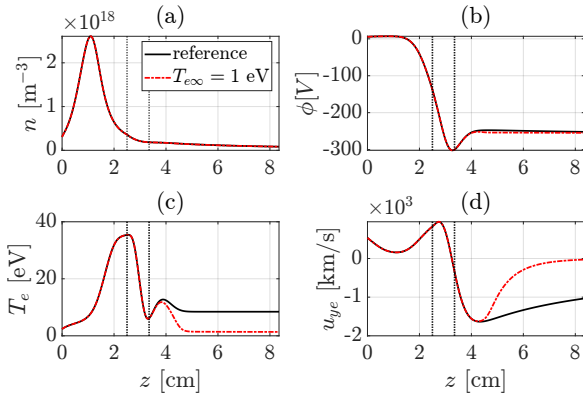
Figure 10: Stationary axial response of reference (black solid line) and $T_{e\infty} = 1$ eV cases (red dash-dotted line). Black dotted vertical lines denote, from left to right, respectively, the location of the exit (point E) and the cathode center (point N).

The low value $T_{e\infty}$ makes also that the work done by the pressure in (Eq. 23) and (Eq. 24) gets diminished and the conversion of electron thermal energy into ion kinetic energy is spatially slower. In figure 11, the axial evolution of ϕ and

$$P_e \equiv A \left(\frac{5}{2} n_e T_e u_{ze} + q_{ze} \right) \qquad \text{(Eq. 28)}$$

are represented. As anticipated, dP_e/dz (this is, the right-hand side of (Eq. 24)), is much smaller in the case with lower $T_{e\infty}$. The result is a much weaker plume electric field and, thus, a lesser acceleration of ions.

It is striking that the temperature profile is very flat downstream even when not imposing $(dT_e/dz)_\infty =$

0. Although barely visible in figure 10(c), there is a small non-zero temperature gradient in the plume. The large thermal conductivity (see (Eq. 10))

$$\kappa = \frac{5 p_e}{2 m_e \nu_e} \frac{1}{1 + \chi^2} \qquad \text{(Eq. 29)}$$

in the plume (due to $\chi \approx 0$ and very low ν_e) makes q_{ze} quite sensitive to temperature gradients. At the same time, q_{ze} has an influence on T_e through the internal energy equation (Eq. 9). Therefore, the large plume value of κ explains that an imperceptibly small difference in $(dT_e/dz)_\infty$ may produce large changes in $T_{e\infty}$, as seen in figure 10. This could explain also why $T_{e\infty}$ seems to be quite sensitive to almost every analysis carried out through the article.
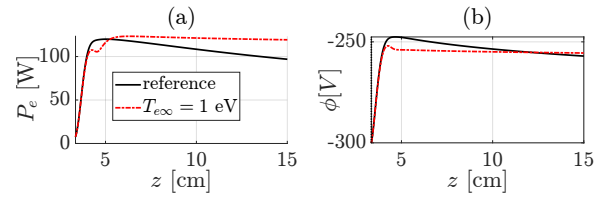
Figure 11: Stationary axial evolution, past the cathode, of ϕ and P_e in the reference (black solid line) and $T_{e\infty} = 1$ eV cases (red dash-dotted line).

4. CONCLUSIONS

In this article we considered an axial stationary model of a Hall-thruster discharge, including the chamber, near plume and far-field regions. Previous works [20–22] used an infinitely thin cathode model to study the interior region from the anode to the cathode and disregarding some other physical effects, such as azimuthal electron inertia. In reference [6], devoted mainly to global instabilities, a similar model was used but incorporating inertia in the azimuthal momentum balance. The equilibrium solutions computed there show that inertia may be important, mainly, close to the anode and cathode regions. Here a finite cathode model is also included and the simulation domain is extended into the far-field region.

If the far-field boundary is placed far enough, the solutions include the plume demagnetization, after which the azimuthal momentum equation is a balance of inertia and collisional forces. The value of $|u_{ye}|$ decays collisionaly in the plume with a rate that can be easiliy correlated to the far-field electron temperature $T_{e\infty}$. For the typical solutions considered in this work, colder plumes lead to faster decay rates due to the dominance of electron-ion Coulomb collisions at low $T_{e\infty}$. The electron thermal conductivity in the unmagnetized plume becomes several orders of magnitude greater than values in the chamber making $T_{e\infty}$ quite sensitive to changes in the model

and in the parameters. Regarding the energy balance, in the expanding plume the electron thermal energy flux decreases and this translates into ion acceleration. On the other hand, the interior part of the solutions seems to be quite robust to the far-field boundary conditions and other minor changes.

The distance from the cathode center to the far-field boundary ($L_{N\infty}$) is considered as one of the parameters of the problem, although it must be large enough so that the solutions become independent of it. The slow decay of $|u_{ye}|$ and the sensitivity of $T_{e\infty}$ requires that the far-field boundary is placed very far (in our reference case, $L_{N\infty} = 40$ cm) in order to reach a decent degree of independence.

When comparing with inertialess solutions, accounting for the electron flow transition across the cathode mitigates, in the vicinity of the cathode, the lack of electron inertia terms; because both solutions satisfy that $u_{ye} = 0$ when $u_{ze} = 0$ (that is promoted by the cathode electron source) and the gradient $\mathrm{d}u_{ye}/\mathrm{d}z$ is smoothed. In view of recent studies on turbulent cross-field transport, we test a rippled turbulent profile $\alpha_t(z)$, that induces large gradients of u_{ye}. This enhances the role of electron inertia, that attenuates the amplitude of u_{ye} ripples. On the other hand, the presence of ripples in u_{ye} and other plasma variables may produce drift-gradient instabilities. An stability study, using equilibrium solutions presented here, is left as future work.

5. ACKNOWLEDGMENTS

6. REFERENCES

[1] Boeuf, J., "Tutorial: Physics and modeling of Hall thrusters," J. Applied Physics, Vol. 121, No. 1, 2017, pp. 011101.

[2] Taccogna, F. and Garrigues, L., "Latest progress in Hall thrusters plasma modelling," Reviews of Modern Plasma Physics, Vol. 3, No. 1, 2019, pp. 12.

[3] Escobar, D. and Ahedo, E., "Low frequency azimuthal stability of the ionization region of the Hall thruster discharge. I. Local analysis," Physics of Plasmas, Vol. 21, No. 4, 2014, pp. 043505.

[4] Smolyakov, A., Chapurin, O., Frias, W., Koshkarov, O., Romadanov, I., Tang, T., Umansky, M., Raitses, Y., Kaganovich, I., and Lakhin, V., "Fluid theory and simulations of instabilities, turbulent transport and coherent structures in partially-magnetized plasmas of ExB discharges," Plasma Physics and Controlled Fusion, Vol. 59, 2017, pp. 014041.

[5] Litvak, A. and Fisch, N., "Resistive instabilities in Hall current plasma discharge," Physics of Plasmas, Vol. 8, No. 2, 2001, pp. 648–651.

[6] Bello-Benítez, E. and Ahedo, E., "Axial-azimuthal, high-frequency modes from global linear-stability model of a Hall thruster," Plasma Sources Science and Technology, 2021.

[7] Escobar, D. and Ahedo, E., "Low frequency azimuthal stability of the ionization region of the Hall thruster discharge. II. Global analysis," Physics of Plasmas, Vol. 22, 2015, pp. 102114.

[8] Romadanov, I., Smolyakov, A., Raitses, Y., Kaganovich, I., Tian, T., and Ryzhkov, S., "Structure of nonlocal gradient-drift instabilities in Hall ExB discharges," Physics of Plasmas, Vol. 23, 2016, pp. 122111.

[9] Sorokina, E. A., Marusov, N. A., Lakhin, V. P., and Ilgisonis, V. I., "Discharge Oscillations in Morozov's Stationary Plasma Thruster as a Manifestation of Large-Scale Modes of Gradient Drift Instability," Plasma Physics Reports, Vol. 45, No. 1, 2019, pp. 1.

[10] Ducrocq, A., Adam, J., Héron, A., and Laval, G., "High-frequency electron drift instability in the cross-field configuration of Hall thrusters," Physics of Plasmas, Vol. 13, 2006, pp. 102111.

[11] Cavalier, J., Lemoine, N., Bonhomme, G., Tsikata, S., Honoré, C., and Grésillon, D., "Hall thruster plasma fluctuations identified as the E×B electron drift instability: Modeling and fitting on experimental data," Physics of Plasmas, Vol. 20, No. 8, 2013, pp. 082107.

[12] Lafleur, T., Baalrud, S., and Chabert, P., "Characteristics and transport effects of the electron drift instability in Hall-effect thrusters," Plasma Sources Science and Technology, Vol. 26, 2017, pp. 024008.

[13] Jandovitz, P., Swanson, C., Matteucci, J., Oliver, R., Pearcy, J., and Cohen, S. A., "Demonstration of fast-electron populations in a low-pressure, low-power, magnetized RF plasma source," Physics of Plasmas, Vol. 25, No. 3, 2018, pp. 030702.

[14] Janhunen, S., Smolyakov, A., Sydorenko, D., Jimenez, M., Kaganovich, I., and Raitses, Y.,

"Evolution of the electron cyclotron drift instability in two-dimensions," Physics of Plasmas, Vol. 25, No. 8, 2018, pp. 082308.

[15] Lafleur, T. and Chabert, P., "The role of instability-enhanced friction on 'anomalous' electron and ion transport in Hall-effect thrusters," Plasma Sources Science and Technology, Vol. 27, 2017, pp. 015003.

[16] Charoy, T., Boeuf, J. P., Bourdon, A., Carlsson, J. A., Chabert, P., Cuenot, B., Eremin, D., Garrigues, L., Hara, K., Kaganovich, I. D., Powis, A. T., Smolyakov, A., Sydorenko, D., Tavant, A., Vermorel, O., and Villafana, W., "2D axial-azimuthal particle-in-cell benchmark for low-temperature partially magnetized plasmas," Plasma Sources Science and Technology, Vol. 28, No. 10, 2019, pp. 105010.

[17] Chapurin, O., Smolyakov, A., Hagelaan, G., Boeuf, J., and Raitses, Y., "Fluid and hybrid simulations of the ionization instabilities in Hall thruster," 36th International Electric Propulsion Conference, No. IEPC-2019-762, Electric Rocket Propulsion Society, Fairview Park, OH, Vienna, Austria, 2019.

[18] Sahu, R., Mansour, A., and Hara, K., "Full fluid moment model for low temperature magnetized plasmas," Physics of Plasmas, Vol. 27, No. 11, 2020, pp. 113505.

[19] Hara, K., "Non-oscillatory quasineutral fluid model of cross-field discharge plasmas," Physics of Plasmas, Vol. 25, No. 12, 2018, pp. 123508.

[20] Ahedo, E., Martínez-Cerezo, P., and Martínez-Sánchez, M., "One-dimensional model of the plasma flow in a Hall thruster," Physics of Plasmas, Vol. 8, 2001, pp. 3058–3068.

[21] Ahedo, E., Gallardo, J., and Martínez-Sánchez, M., "Model of the plasma discharge in a Hall thruster with heat conduction," Physics of Plasmas, Vol. 9, No. 9, 2002, pp. 4061–4070.

[22] Ahedo, E., Gallardo, J., and Martínez-Sánchez, M., "Effects of the radial-plasma wall interaction on the axial Hall thruster discharge," Physics of Plasmas, Vol. 10, No. 8, 2003, pp. 3397–3409.

[23] Bittencourt, J., Fundamentals of plasma physics, Springer, Berlin, Germany, 2004.

[24] Boeuf, J. and Garrigues, L., "Low frequency oscillations in a stationary plasma thruster," J. Applied Physics, Vol. 84, No. 7, 1998, pp. 3541–3554.

[25] Hagelaar, G., Bareilles, J., Garrigues, L., and Boeuf, J., "Role of anomalous electron transport in a stationary plasma thruster simulation," Journal of Applied Physics, Vol. 93, No. 1, 2003, pp. 67–75.

[26] Koo, J. W. and Boyd, I. D., "Modeling of anomalous electron mobility in Hall thrusters," Physics of Plasmas, Vol. 13, No. 3, 2006, pp. 033501.

[27] Tsikata, S. and Minea, T., "Modulated electron cyclotron drift instability in a high-power pulsed magnetron discharge," Physical Review Letters, Vol. 114, 2015, pp. 185001.

[28] Tsikata, S. and Hara, K., "Plasma instabilities in cross-field configuration: an analysis of the relevance of different modes for electron transport," 36th International Electric Propulsion Conference, No. IEPC-2019-758, Electric Rocket Propulsion Society, Fairview Park, OH, Vienna, Austria, 2019.

[29] Lakhin, V. P., Ilgisonis, V. I., Smolyakov, A. I., Sorokina, E. A., and Marusov, N. A., "Effects of finite electron temperature on gradient drift instabilities in partially magnetized plasmas," Physics of Plasmas, Vol. 25, 2018, pp. 012106.

[30] Frias, W., Smolyakov, A., Kaganovich, I., and Raitses, Y., "Long wavelength gradient drift instability in Hall plasma devices. I. Fluid theory," Physics of Plasmas, Vol. 19, 2012, pp. 072112.